Including Tides Improves Subtidal Prediction in a Region of Strong Surface and Internal Tides and Energetic Mesoscale Circulation

Colette G. Kerry[1] and **Brian S. Powell[2]**

[1]UNSW Australia, Sydney, NSW, Australia, [2]University of Hawai'i at Manoa, Honolulu, HI, USA

Abstract Model predictions of the oceanic subtidal circulation have typically excluded the tides, assuming that tides have little influence on subtidal flows. The deterministic surface (barotropic) tide can be removed from observations for assimilation, yet the surface tides may have important impacts on subtidal circulation in shelf regions with flow-on effects to the deep ocean. Internal (baroclinic) tides are non-deterministic so must be included as observation error for assimilation if they are not resolved by the model. Using Twin Experiments with 4-D Variational Data Assimilation, we examine the influence of the principal semidiurnal (M_2) tide on the predictability of the subtidal ocean circulation in the South China and Philippine Seas. We find that including tides in our model significantly improved subtidal predictions across the region. This results from both the influence of tidal dynamics on the subtidal circulation, and from higher prior errors prescribed to the observations when the model does not resolve the internal tide signal. The tides are particularly important for predictions of temperature in the South China Sea and Kuroshio Current where tidal mixing influences water mass properties. In the Philippine Sea deep basin, improved predictability results from resolving the internal tides allowing smaller prior errors to be prescribed to the assimilated Sea Surface Height and subsurface observations. This study illustrates the importance of including tides to accurately predict subtidal circulation in a region of strong surface and internal tides and energetic mesoscale circulation and including a significant Western Boundary Current region.

Plain Language Summary Modeling systems that predict the general wind-driven eddying circulation in the ocean typically do not include tides, assuming tides have little influence on these more slowly varying flows. These prediction systems require both a numerical ocean model and ocean observations that are combined in an optimal way to achieve the ocean forecasts. When combining observations with a model it is crucial to understand and account for the processes resolved by each. In this work we design experiments to test the influence of including, or not including, the tides on prediction of the low frequency flows. Our results show the importance of including tides to accurately predict the general ocean circulation in a region of strong surface and internal tides and energetic eddying circulation and including a significant Western Boundary Current region. The tides improve predictions of temperature in the South China Sea and Kuroshio Current where tidal mixing is important. In the Philippine Sea deep basin, improved prediction results from resolving the tidal variability captured by the observations.

1. Introduction

Effective prediction of the oceanic circulation uses data assimilation techniques to combine ocean observations with a dynamical model. The goal of data assimilation is to produce a state estimate that represents the observations within the dynamical context of the model and minimizes the difference between the observations and the model, given prior assumptions of the uncertainties of both. Forecasts of the mesoscale ocean circulation are highly sensitive to the initial state and both deterministic, variational data assimilation methods (Courtier et al., 1994; Di Lorenzo et al., 2007; Moore et al., 2004, 2011; Powell et al., 2008) and statistical, ensemble methods (Houtekamer & Mitchel, 1998; Oke et al., 2005, 2008) reduce the error in the initial state at the beginning of each forecast cycle. The configuration of the dynamical model should be governed by the relevant physical processes and, when combining observations with the model, it is important to understand and account for the processes resolved by each. Constraining ocean circulation models given observational data, that are limited by the temporal and spatial scales observed and that sample processes that may not be captured in the model, requires careful formulation of the prior hypotheses about errors in the model background and the observations.

It is now well understood that the eddying mesoscale circulation and its associated varying stratification is required for the prediction of internal tides (Arbic et al., 2010; Kerry et al., 2014a; Shriver et al., 2012), yet the influence of the surface and internal tides on mesoscale prediction is not well studied or understood. The atmospherically-forced eddying general ocean circulation has typically been simulated without tides and the major global ocean forecast models (e.g., Chassignet et al. (2009)) do not yet include tides in their public releases. Omitting the tides may influence subtidal prediction in two ways. Firstly, by not including tides we make the inherent assumption that the tidal and subtidal dynamics are independent; however the surface tides may have important impacts on subtidal circulation in shelf regions with flow-on effects to the deep ocean (e.g., Li et al. (2020)). Secondly, the deterministic barotropic tides can be removed from the observations for assimilation; yet, the internal tides include a significant non-deterministic component (Kerry, Powell, & Carter, 2016; Shriver et al., 2014) and in most cases the tidal signal cannot be completely removed from the observations. In regions of energetic and highly varying internal tides, such as the Philippine Sea (Kerry et al., 2014a; Pickering et al., 2015; Shriver et al., 2014; Simmons et al., 2004), this unresolved internal tide signal may be large and must be included in the prior errors associated with the observations thus limiting their value.

In this study, we investigate the influence of the tides on the predictability of the subtidal ocean circulation in a region that experiences both dynamic mesoscale circulation and energetic internal tides. The Philippine Sea region provides an ideal case-study for this work as it exhibits strong internal tides (Alford et al., 2011, 2015; Ramp et al., 2004), tidal mixing in the South China Sea (SCS) (Li et al., 2020), the origins of an important Western Boundary Current system (Rudnick et al., 2011; Yuan et al., 2006) and high eddy activity due to baroclinic instability between the Subtropical Counter Current and the North Equatorial Current (Qiu & Chen, 2010).

We develop Twin Experiments, based on a realistic observing system, to examine the importance of including the tides in making state estimates and predictions of the subtidal circulation in the region. For the data assimilation we use Incremental Strong-constraint 4-dimensional Variational Data Assimilation which minimizes the difference between the model solution of the time-evolving flow and all available observations over the assimilation interval, based on prior assumptions of the errors in the observations and the model background state (Di Lorenzo et al., 2007; Moore et al., 2004, 2011). We focus on short-range predictions with 7-day forecast windows. The experimental setup is described in Section 2, we present the impact of including tides on the skill of the state estimates and predictions of subtidal circulation in Section 3, and a discussion of the mechanisms for improvement by including tides is presented in Section 4. Finally, conclusions and the implications for modeling in regions of energetic tides are discussed.

2. Experiment Setup

2.1. Model Configuration

We use the Regional Ocean Modeling System (ROMS) to simulate the atmospherically-forced eddying general circulation and the principal lunar, semidiurnal (M_2) barotropic and baroclinic tides in the Philippine Sea. ROMS is a free-surface, hydrostatic, primitive equation ocean model solved on a curvilinear grid with a terrain-following vertical coordinate system (Shchepetkin & McWilliams, 2005). The ROMS computational kernel is further described in Shchepetkin and McWilliams (1998, 2003). Although internal tides inherently have a non-hydrostatic component, the hydrostatic approximation remains valid for the relatively large scale processes and coarse model resolution used in this study (Bergh & Berntsen, 2009; Vitousek & Fringer, 2011); we focus on the internal tides that propagate into the Philippine Sea deep basin and into the SCS prior to interaction with the shelf. The same model configuration was used in Kerry et al. (2014a, 2014b; Kerry, Powell, & Carter, 2016a) to study the impact of the mesoscale circulation on internal tides in the Philippine Sea.

We focus on the dominant semidiurnal constituent, M_2, so as to be able to present a thorough analysis within the scope of this study. The amplitude of the M_2 barotropic tide is ∼0.6 m in the Philippine Sea and decreases upon strong tidal energy dissipation at the Luzon Strait to ∼0.2 m in the SCS, while the amplitude of the diurnal tide K_1 is ∼0.1–0.2 m in the Philippine Sea and increases to ∼0.2–0.4 m in the SCS basin due to resonance (Zu et al., 2008). The amplitude of S_2 is considerably smaller than that of M_2, while the amplitudes of K_1 and O_1 are comparable. The baroclinic energy fluxes associated with semidiurnal (combined M_2/S_2) and the diurnal (combined K_1/O_1) internal tides generated at the Luzon Strait are of similar magnitude (Alford et al., 2011). Further studies may be interested in investigating the K_1 internal tides or combined constituents.
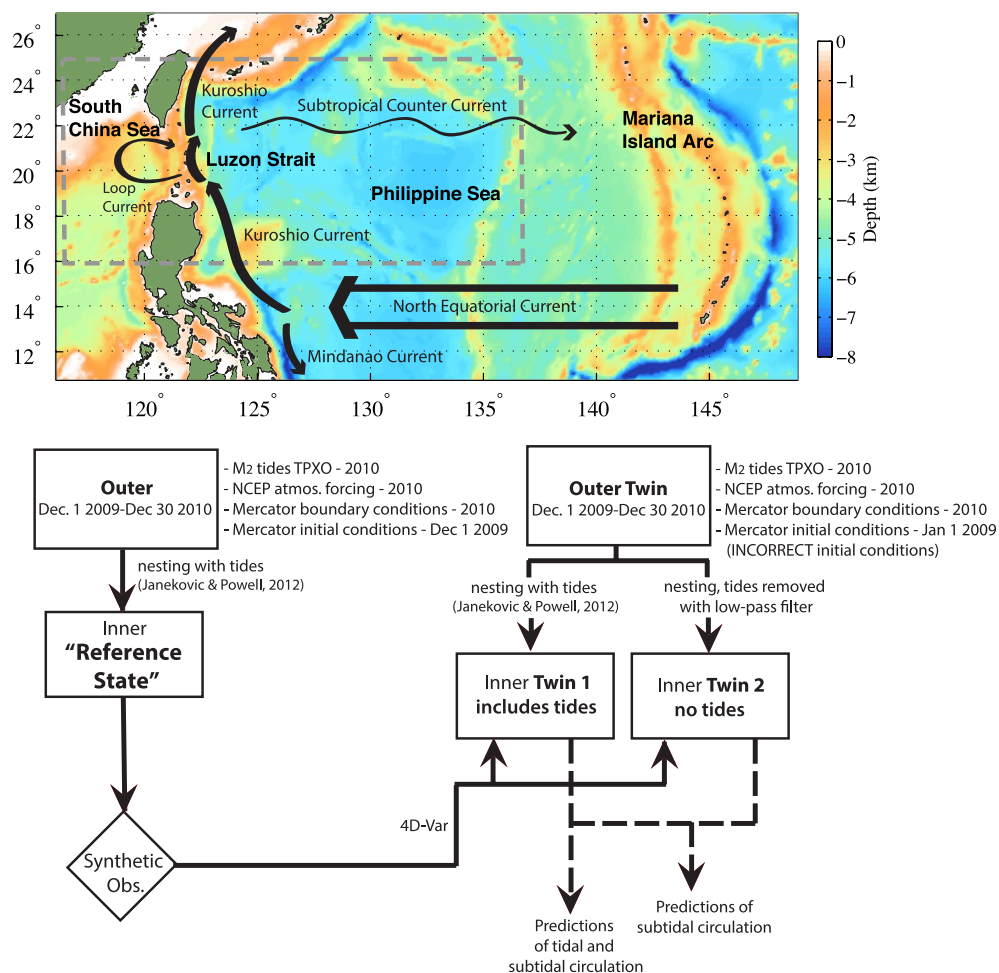
Figure 1. Top: *Outer* model domain with model bathymetry and schematic of the region's wind-driven ocean circulation. The *inner* domain (gray dashed line) used for the experiments is marked. Bottom: Twin Experiment methodology showing *Outer* twins and nested *Inner* twins.

An *Outer* and an *Inner* domain are used as the basis of the Twin Experiments (Figure 1). Both grids have identical bathymetry and horizontal and vertical resolution. The *Outer* grid encompasses both the Luzon Strait and the Mariana Island Arc thus resolves the remotely generated internal tides from the Mariana Arc under varying mesoscale circulation. The *Inner* grid receives boundary conditions from the *Outer* grid and provides a more computationally efficient domain for the data assimilation experiments.

The models have a variable horizontal resolution, with 8 km over most of the domain, and a higher zonal resolution of 4.5 km over the Luzon Strait. This allows improved bathymetric resolution while minimizing pressure gradient errors (D. B. Haidvogel et al., 2000; Haney, 1991; Mellor et al., 1994) in the region of steep topography. The model is configured with 25 vertical s-layers distributed with a higher resolution in the upper 250 m of the water column. We use a bathymetric smoothing method (described in Sikiric et al. (2009)) that places a high priority on maintaining topography (slopes and peak heights) important for internal tide generation (Di Lorenzo et al., 2006). The model bathymetry is obtained from the General Bathymetric Chart of the Oceans one-minute gridded bathymetry data generated from combined satellite-derived gravity data and ship depth soundings (IOC et al., 2003).

In both the *Outer* and the *Inner* models, harmonic mixing of momentum is applied in the horizontal to handle sub-grid scale turbulence and the viscosity is derived from the horizontal divergence of the deviatory stress tensor (Wajsowicz, 1993). The parameters are scaled by grid-size such that less explicit diffusion occurs in the

high-resolution (4.5 km) region than in the 8 km region. The Mellor and Yamada (1982) level-2.5, second-moment turbulence closure scheme (MY2.5) is used in parameterizing vertical turbulent mixing of momentum and tracers.

2.2. Twin Experiment Methodology

Twin Experiments allow us to evaluate the performance of a state estimation and prediction system based on a known ocean state, by defining a given model solution as the *Reference State*. The goal is to assimilate synthetic observations extracted from the *Reference State* into a Twin model, which is initialized from a perturbed state about the *Reference State* allowing us to asses how well the assimilation improves our estimates. Such experiments are useful as we can compare our predictions to a known state, compared to prediction studies of the real ocean where the ocean state is largely unknown as oceanic observations are typically sparse in time and space.

In this work we perform two experiments: one that includes the tides and one that does not. The experiments assimilate synthetic observations that are representative of the realistic observations that were available in the Philippine Sea region. Both experiments assimilate the same set of observations; however, there are differences in the prescribed prior observations errors, which are designed to account for the oceanic processes that are unresolved by the model. We compare the predictions of subtidal circulation for these two experiments to demonstrate the impact of including tides on subtidal prediction in the Philippine Sea region.

2.2.1. The Reference State

We define the free-running simulation of 2010 that resolves the M_2 internal tides and the varying sub-tidal circulation as the *Reference State* described below and shown in Figure 1. The *Outer* model uses boundary and initial conditions from the MERCATOR general ocean circulation model provided by Mercator Océan of France (www.mercator-ocean.eu). The atmospheric forcing was provided by the National Center for Environmental Prediction's (NCEP) reanalysis atmospheric model to simulate the atmospherically-forced eddying ocean circulation (Kistler et al., 2001). The M_2 tides are included by forcing at the four open boundaries with M_2 tidal surface elevation and momentum from the global barotropic tidal model provided by the Oregon State University TOPEX/Poseidon Global Inverse Solution, TPXO7.1, (Egbert & Erofeeva, 2002). The *Reference State* is defined as a simulation performed on the *Inner* domain in which the general ocean circulation and baroclinic tides are applied at the boundaries through nesting with the *Outer* domain simulation. We use the method for nesting tidal models described in Janekovic and Powell (2012).

The *Reference State* simulation includes the influence of baroclinic tides generated at the Mariana Arc under the varying sub-tidal dynamics, which was shown to be significant by Kerry et al. (2014a), and is equivalent to the *Full* case described in that publication. The *Reference State* provides a good representation of the subtidal and tidal ocean circulation by comparison with a variety of observations and previous modeling and observation-based studies. For detailed validation of the model's mean flow, mesoscale eddy related variability and surface and internal tide representation the reader is referred to Kerry et al. (2014a).

2.2.2. The Twin Experiments

We assimilate synthetic observations, generated from the time and location of actual observations (see below), into two models that are initialized from a perturbed state about the *Reference State* and that differ from each other in that they do and do not include the tides. The methodology is described in the flow diagram in Figure 1. The *Outer Twin* is initialized from perturbed initial conditions (from Mercator on 1 Jan 2009, rather than 1 Dec 2009). The free-running *Outer Twin* does not converge with the *Outer* simulation over the 1-year simulation period, indicating that the initial conditions continue to dominate, rather than the boundary or atmospheric forcings, and that data assimilation is required to correct the ocean state estimates. This "initial value problem" is typical of ocean mesoscale prediction, in which errors in the initial conditions dominate the forecast errors (e.g., Thoppil et al. (2021)).

Tide experiment on the *Inner* domain simulates the subtidal dynamics and the M_2 internal tides, while *No-Tide* experiment simulates the sub-tidal dynamics but does not include the tides. For both experiments the assimilation is completed for 13 months, with the first month omitted from the analysis for baroclinic tide spin-up. The spin-up of the baroclinic tides was shown to take 30 days in Kerry et al. (2013) (their Figure 11), corresponding to the time for Modes 1-3 to reach the Luzon Strait from the Mariana Arc.

2.3. Data Assimilation Configuration

2.3.1. Incremental Strong-Constraint 4D-Var

We use Incremental Strong-constraint 4-dimensional Variational Data Assimilation (IS4D-Var) to combine the observations and the modeled ocean state to produce an improved ocean state estimate. This technique uses variational calculus techniques to solve for the increments in model initial conditions, boundary conditions and forcing such that the difference between the modeled solution and all available observations is minimized - in a least-squares sense - over the assimilation window (Moore et al., 2004, 2011). IS4D-Var has been used successfully to provide improved state estimates in complex oceanic regions (Kerry, Powell, Roughan, & Oke, 2016; Powell et al., 2008; Souza et al., 2014).

The goal is to solve for the nonlinear ocean solution that is dynamically consistent with the observations and is free within the known uncertainties in the system. As such, the prior assumptions of the uncertainties in the observations (prior observation errors, see Section 2.3.2) and the model background state (prior background error covariances, see Section 2.3.3) are key to achieving an optimum combination of the model and the observations. In this work, we examine the role of the observation uncertainty for unresolved physics.

2.3.2. Observations and Prior Observation Errors

For the Twin Experiments, we generate synthetic observations by sampling the *Reference State* for the same observation types and locations as the observations that were available within the existing observing system in the Philippine Sea. The assimilation experiments are performed for 2010, the year of the PhilEx observational campaign (Gopalakrishnan et al., 2021a, 2021b; Worcester et al., 2012). Other available sub-surface observations and satellite-derived surface observations are also sourced for this time period. The sub-surface observation locations and times are shown in Figures 2a and 2b. The number of temperature observations outweighs the number of observations of each of the other state variables (Sea Surface Height (SSH), zonal and meridional velocities and salinity) by an order of magnitude (Figure 2d). Temperature observations are dominated by Sea Surface Temperature (SST) data, followed by the high-frequency mooring data from moorings T1-5 and the Distributed Vertical Line Array (DVLA) (Figure 2e). The actual observational data is used to estimate the prior observation errors.

The prior observation errors must account for the instrument error and the error of representativeness. Errors of representativeness can come about due to the spatial and temporal discretization in the model; for example, if several observations exist in the same grid cell taken within the same time-step, the error of representativeness is computed by the variance of these coinciding observations. Because our synthetic observations are derived from the *Reference State* model which has identical discretization as the Twin Experiments, no such errors exist here. Errors of representativeness must also account for any physical processes that may be sampled by the observations but are not resolved in the model; the (lack of) internal tides in *No-Tide* is an example of this.

The synthetic observations assimilated in *Tide* and *No-Tide* are identical except the SSH, where TPXO7.1 is used to remove the barotropic tidal signal for *No-Tide* and the Acoustic Doppler Current Profiler (ADCP) velocities, which are low-pass filtered to remove the semidiurnal frequencies and higher for *No-Tide*. The high frequency temperature and salinity observations from the moorings are not filtered to remove the tides, to be consistent with the other temperature and salinity observations for which we are unable to remove the tidal signal. The specified observation errors for SSH and subsurface temperature and salinity are different for *Tide* and *No-Tide* because *No-Tide* must account for the unresolved internal tide signal, requiring higher errors. The synthetic observations are then perturbed with a random error such that the errors are normally distributed within the bounds of the observational error of the actual observations. The observations used are described below.

SSH: We generate synthetic SSH observations applied daily and gridded at 1/3° x 1/3° to mimic the data available from Archiving, Validation and Interpretation of Satellite Oceanographic Data (AVISO), France (CNES, 2015). The inherent error in AVISO data is specified as 3 cm. For the experiment that resolves the internal tides (*Tide*), this is the specified SSH error over the entire domain. For *No-Tide* we remove the barotropic tidal signal as predicted by TPXO7.1 from the SSH synthetic observations. As such, the SSH observations include the internal tide surface expression, which is not resolved by *No-Tide* or predicted in TPXO7.1, as well as any error in the TPXO7.1 barotropic SSH predictions compared to the *Reference State*. This unresolved signal must be accounted for in the prior observational errors. The SSH error that is added (in quadrature) to the 3 cm product error for
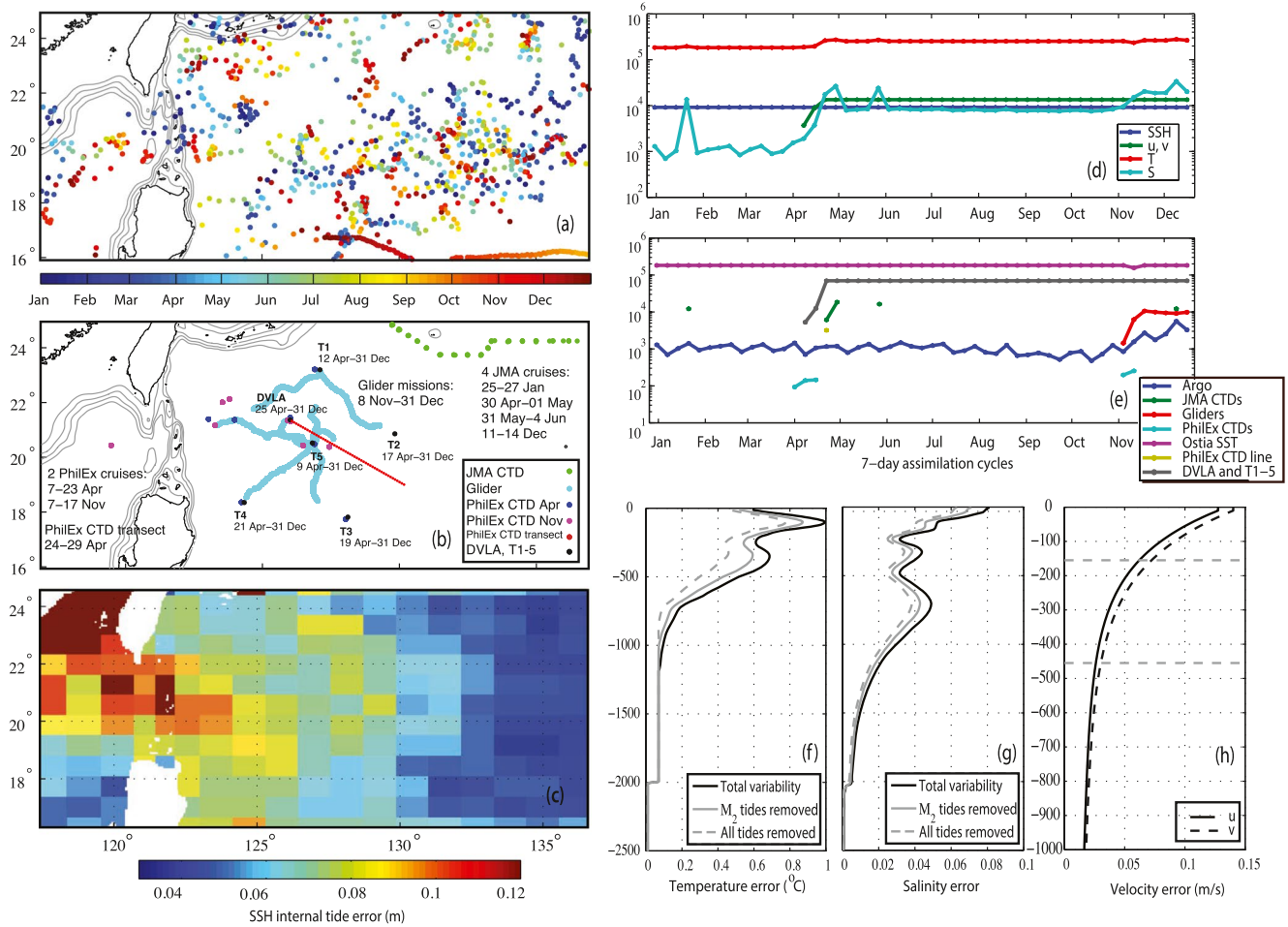
Figure 2. Subsurface observations for 2010: (a) Argo floats and (b) other subsurface observations. Note: These are the subsurface observations available in the region for 2010 and represent the observation types and locations that are used to generate synthetic observations from the *Reference State*. (c) Sea Surface Height (SSH) error due to not resolving the internal tides and using TPXO7.1 to attempt to remove the tidal signal from the SSH observations for *No-Tide*. (d) Number of observations broken down by state variable and (e) number of temperature observations broken down into observation provenance. (f) Vertical prior observation error profiles of Temperature for *No-Tide* (where the errors account for the Total variability) and *Tide* (where the errors account for the variability with the M_2 tides removed). Error profiles that account for the variability with all tidal constituents removed are also shown for reference. (g) Same as (f) but for Salinity. (h) Error profiles of zonal (*u*) and meridional (*v*) velocities.

No-Tide is shown in Figure 2c. To compute these errors we calculate the SSH amplitudes and phases at the M_2 frequency over five M_2 tidal cycles (62 hr) every 3 days from the *Reference State*. We choose 3 days as it is long enough to extract the M_2 amplitude and phase (using 5 tidal cycles) and short enough that the mesoscale circulation is likely to vary little, therefore capturing the variability in internal tide surface expression due to varying mesoscale circulation over the simulation period. We then compute the absolute RMS error, E, between the *Reference State* and TPXO7.1 at the M_2 frequency for every 3-day realization, given by

$$E = \sqrt{\frac{1}{2}\left(A_o^2 + A_m^2\right) - A_o A_m \cos\left(G_o - G_m\right)}, \qquad (1)$$

where subscripts *o* and *m* denote observed and modeled amplitudes (A) and phases (G), respectively. We take the mean E over the 120, 3-day periods and then take the maximum of the mean E values in approximately 1° squares. This last step removes the variability at the Mode-1 internal tide wavelength scale. The values represent the mean internal tide SSH expression, encompassing both the stationary and non-stationary internal tides.

SST: We mimic the daily gridded (0.054° by 0.054°) SST data product produced by the UK Meteorological Office, the Operational SST and Sea Ice Analysis (OSTIA, Stark et al. (2007)). The OSTIA product combines

satellite data from a variety of sensors and in situ data from drifting and moored buoys using optimal interpolation and has an estimated product error of 0.3°C. This error is specified as the SST observational error over the entire domain for *Tide* and *No-Tide* for our synthetic SST data. The SST data is assimilated once per day, at 2 a.m. local time.

Subsurface data: Synthetic subsurface observations are generated to mimic the platforms available in the Philippine Sea:

Argo floats: Argo is an international program consisting of free-drifting profiling floats that measure the temperature and salinity of the upper 2000 m of the ocean (www.argo.ucsd.edu). The Argo float locations and times in our model domain for 2010 are shown in Figure 2a.

Japan Meteorological Agency (JMA) CTDs: Repeat Conductivity Temperature Depth (CTD) survey sections were maintained by JMA (refer to Qiu et al. (2012)), down to 4600 m. Four cruises took place in 2010 (green dots in Figure 2b).

PhilEx Glider missions: Autonomous gliders were deployed from 8 November 2010 into 2011 (cyan in Figure 2b), measuring temperature and salinity in the upper 1000 m.

PhilEx Moorings and DVLA: Five moorings (T1-5) and a DVLA were installed as part of PhilEx to the east of the Luzon Strait (black crosses in Figure 2b) from the April 2010 to April 2011. Instruments spaced vertically along the moorings took temperature and salinity measurements at high sampling frequencies (5–20 min intervals). An ADCP was also located on each of T1-5 measuring current velocities.

PhilEx CTD sensors: Ship-borne CTD sensors were deployed on two separate cruises in April and November (blue and magenta circles in Figure 2b, respectively) and measured temperature and salinity to below 5000 m depth. A transect was made from the DVLA location to a station located at 19.00°N, 130.20° E during which CTDs were taken every 10 km (red circles in Figure 2b).

Subsurface temperature and salinity errors: The observational errors specified for the synthetic subsurface temperature and salinity observations vary with depth and are prescribed as a fraction of profiles of typical variability (Figures 2f and 2g). We used subsurface data from Argo for 2009–2012, JMA CTDs for 2009–2012 and PhilSea glider and CTD data from 2010 to 2011 to calculate the mean of the 30-day running standard deviations to give a single variability profile for the entire domain for temperature and salinity, describing the *typical variability* (with tides) across the domain.

To devise the temperature and salinity error profiles for the experiments that do and do not resolve the M_2 internal tides, we make use of the only subsurface data that was available to us at tide-resolving frequency; the temperature data from the DVLA between 180 and 1178 m. By comparing the variability profiles for the raw DVLA data with variability profiles of the DVLA data filtered to remove the semidiurnal tides, we produce an estimate of the subsurface variability associated with the internal tide.

The temperature error profile accounting for the unresolved internal tide (prescribed to *No-Tide*, black solid line in Figure 2f) is given by the variability profile from the unfiltered DVLA data over the depth range of the DVLA (180–1178 m). For the upper 180 m, we scaled the temperature *typical variability* profile described above by 0.4 such that it best matched the DVLA temperature variability profile. Below 1178–2000 m we specify an error of 0.07°C, and below 2000 m the error is set to 0.01°C, also estimated based on the scaled *typical variability* profile. The temperature error profile for *Tide* (which resolves the M_2 tides, gray solid line in Figure 2f), is computed using the filtered DVLA data (with the semidiurnal tides removed). The temperature *typical variability* profile scaled by 0.35 is used for the upper 180 m. The errors below 1178 m are identical to those prescribed in *No-Tide* as isotherm displacement due to internal tides is small at these depths. The variability profile with all tidal constituents removed is also shown in Figure 2f for reference. Salinity observations were not available at the DVLA, so to obtain the salinity error profiles (Figure 2g) we scale the salinity *typical variability* profile as we did for temperature, by 0.4 and 0.35 to give error profiles for *No-Tide* and *Tide* respectively (black and gray lines in Figure 2g).

Subsurface velocity errors: The ADCP data was not available to us, so in order to devise velocity typical variability profiles we make use of a free-running model simulation for 2010 that simulates the general ocean circulation without the tides. We use output from this simulation in the region of the DVLA and T1-5 (17.5–23.2°N and

124.2–129.9°E) and generate profiles of the mean of 30-day running standard deviations with depth for zonal (u) and meridional (v) velocities. These profiles represent typical variability without tides and are appropriate prior observation error profiles for both *Tide* and *No-Tide*. *No-Tide* does not resolve the tides but we filter the ADCP data before assimilation to remove tidal variability.

2.3.3. Assimilation System Configuration

We estimate the prior background error covariances as described in Weaver and Courtier (2001). The background error covariances are kept constant over the year-long assimilation and consistency checks show that the prior and posterior background errors are consistent. We find that 15 *inner* loops and one *outer* loop gives an acceptable reduction in the cost function for an acceptable computational cost. For effective error reduction in the nonlinear model solution, the assimilation window must be sufficiently short such that the tangent linear assumption remains acceptable. We find that the tangent linear assumption remains reasonably valid for realistic perturbations over 7 days, so the analysis window is chosen to be 7 days.

3. State Estimates and Predictions of Subtidal Circulation

3.1. Correlations in Observation Space

We begin with simple correlations to examine how well our state estimates (the analyses) match the *Reference State* observations for the two experiments, *Tide* and *No-Tide*. Figure 3 shows scatter plots of the *Reference State* versus *Tide* and *No-Tide* analysis model output at the observation locations for SSH, SST, subsurface temperature and salinity. *Tide* achieves significantly better SSH estimates by including the tides, compared to *No-Tide* that does not resolve the tides and uses TPXO7.1 to remove the tidal signal from the SSH observations. SST estimates are also slightly better for *Tide*. The notable outliers in *No-Tide* SST, where the model is too warm, correspond to data points in the SCS (refer to Section 4.1). The subsurface temperature and salinity observations include the mooring data (DVLA and T1-5) and all other subsurface observations (Argo, Gliders and CTDs). *Tide* has slightly higher r^2 values compared to *No-Tide* for both subsurface temperature and salinity. The improved match of *Tide* with the *Reference State* as compared to *No-Tide*, is more clearly seen by observing the time-series of the temperature observations at the moorings (Figure 3, right column). *Tide* captures the high frequency variability in the *Reference State* with a reasonable match in amplitude at all depths shown.

3.2. Comparison to *Reference State*

The advantage of the Twin Experiments is that the *Reference* ocean state is known, so the analyses and predictions of the circulation for *Tide* and *No-Tide* can be examined in model space. To examine the forecasts and analyses compared to the *Reference State* we filter the state variables of interest using a 4th-order Butterworth filter to consider the low frequency (LF) and high frequency components separately. The LF component is defined as periods greater than 48 hr (the subtidal circulation) and high frequencies (HF) component is defined as periods less than 15 hr and includes the M_2 tides. Frequency spectra of spatially-averaged kinetic energy (not shown) reveal that fluctuations in the intermediate frequency range (IF, periods of 20–45 hr, including the inertial period and non-tidal diurnal fluctuations) were small compared to tidal fluctuations and fluctuations associated with the LF mesoscale flow for our assimilations. The IF range is therefore not discussed here. The IF errors are also considerably lower than the HF and LF errors (e.g., Figures 5a–5f).

The addition of the filtered components matched the original time-series extremely well with the step changes (between assimilation windows) being represented by more gradual transitions that affected at most the first and last days of the 7-day periods. The match was within 1% excluding the first and last days. As such, for all of the analyses broken down into frequency bands, we exclude the first and last day of each 7-day window.

3.2.1. SSH

SSH observations are available in a uniform grid across the entire domain; however, spatially-varying prior errors in *No-Tide* affect how the assimilation adjusts to fit the observations. The LF SSH state estimates are significantly better for *Tide* compared to *No-Tide* particularly in the Kuroshio and SCS regions (Figures 4a and 4b). The greater analysis errors for the *No-Tide* case are expected as the additional SSH prior error for *No-Tide* is of the order of 8–12 cm near the Luzon Strait and in the SCS (Figure 2c). These errors are of similar order of magnitude
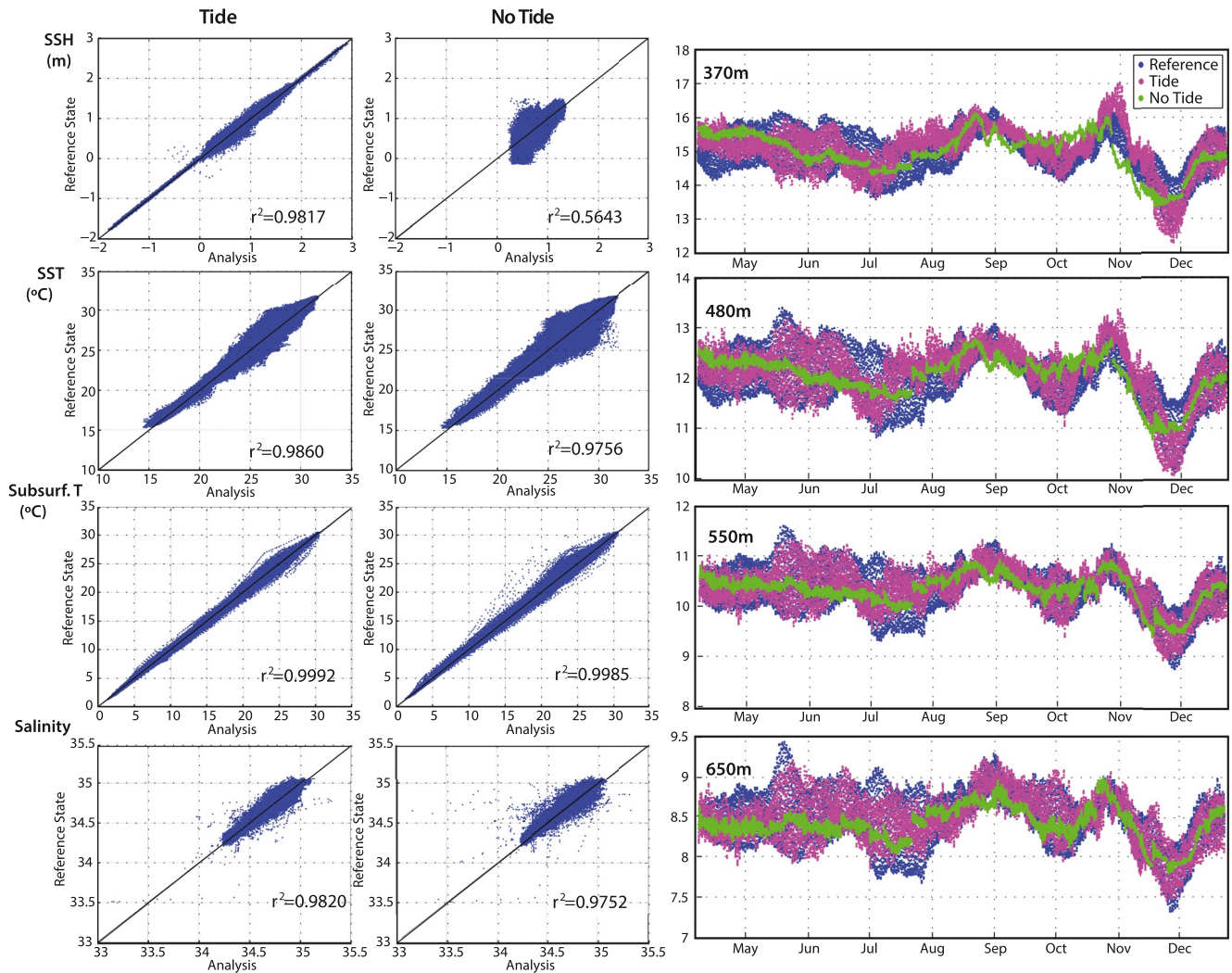
Figure 3. Left and middle columns: *Reference State* versus Analysis at observation locations for Sea Surface Height, Sea Surface Temperature, subsurface temperature and salinity for *Tide* and *No-Tide* with correlation coefficient r² values shown. Right column: Time series of subsurface temperature for mooring T5 observations from the *Reference State Tide* and *No-Tide* analysis.

to the mesoscale signal (refer to Figure 3 from Kerry et al. (2014a)). The Kuroshio region has slightly lower additional prior errors (6–8 cm), but the SSH in this region is tightly coupled to the eddies at the Luzon Strait (Lien et al., 2014) and temperature in the SCS (Mensah et al., 2014; Wu et al., 2017) which are poorly represented in *No-Tide*.

In the Kuroshio and SCS regions, the forecast ands analysis errors are dominated by the LF component and are significantly improved in the *Tide* case (Figures 5b and 5c) compared to the *No-Tide* case (Figures 5e and 5f). In the Kuroshio, the tides are particularly important in the summer and fall months (Figure 5e). In the Philippine Sea, analysis errors range between 4 and 7 cm in *Tide* (Figure 5a) and 6–10 cm in *No-Tide* (Figure 5d) with the LF and HF components having a similar contribution.

3.2.2. SST

SST state estimates and predictions are better for *Tide* than they are for *No-Tide* with the most pronounced differences being in the northern SCS and Kuroshio regions (Figures 4c and 4d for *Tide* and *No-Tide* respectively). Note that SST is not separated into HF and LF as variability at tidal frequencies is not seen in the SST field (as it is for SSH or for subsurface temperature). Unlike the SSH, the prior observation errors applied to SST are identical for *Tide* and *No-Tide*. We suggest that there are two key factors that contribute to the degraded SST predictions
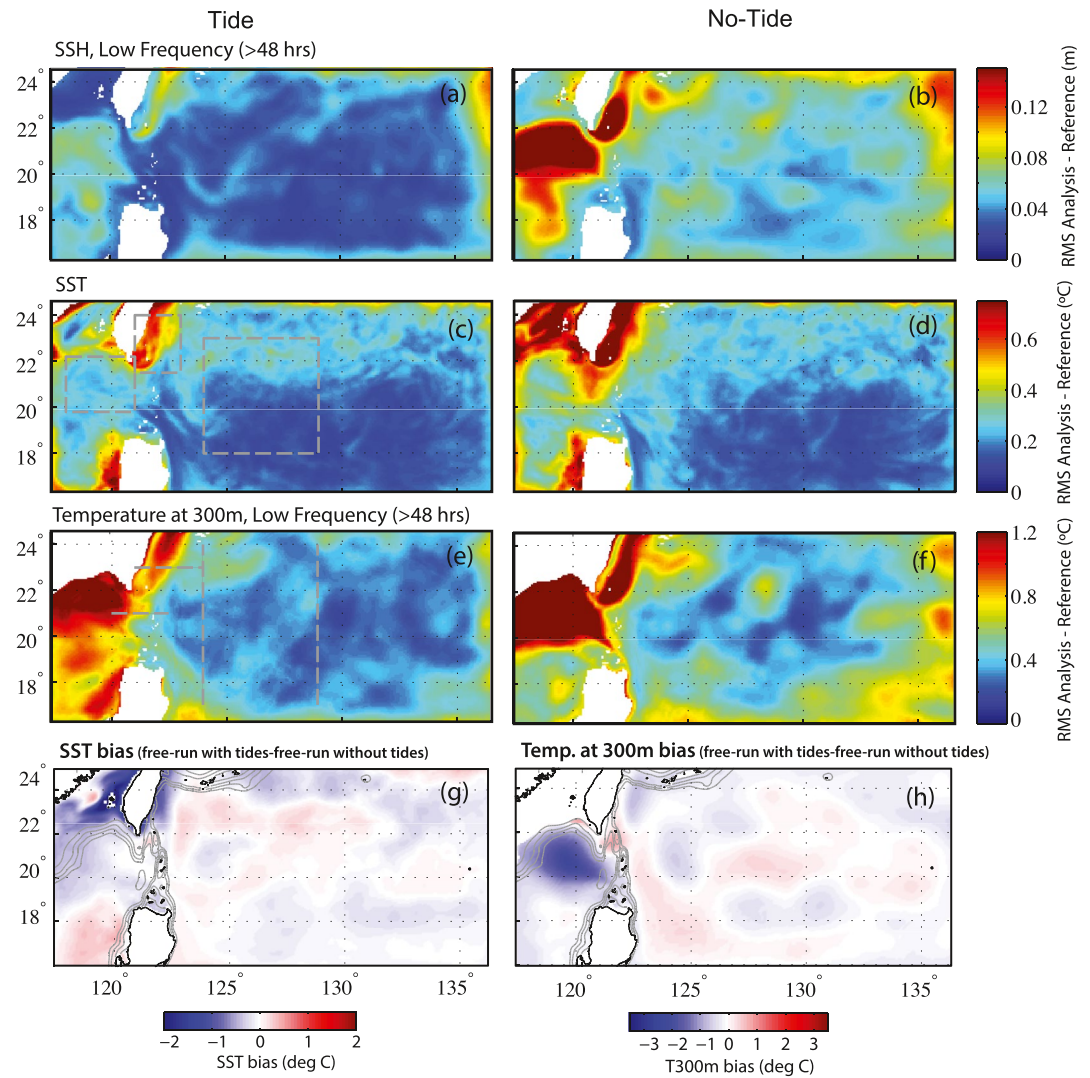
Figure 4. Root-mean squared Analysis-*Reference State* for low frequency (LF) (a–b) Sea Surface Height, (c–d) Sea Surface Temperature (SST), and LF (e–f) T_{300m} for *Tide* (left) and *No-Tide* (right). South China Sea, Kuroshio and Philippine Sea regions used for spatially-averaged error analysis (Figures 5 and 6) are shown by the gray dashed lines in panel (c). Cross sections for error analysis (Figure 5) are shown by gray dashed lines in panel (e). (g) Mean SST and (h) temperature at 300 m from the free-running model with M_2 tides minus mean temperature from the free-running model without tides for 2010.

in *No-Tide*. Firstly, tidal mixing is an important dynamic that controls upper ocean temperature in the Kuroshio and SCS regions in the model (Section 4.1, Figures 4g and 4h). Secondly, the degraded SSH predictions in *No-Tide* (discussed in Sections 4.2 and 4.3) may contribute to the degraded SST predictions through the dynamical connection between SSH and the thermal structure of the upper ocean (e.g., Goni et al. (1996)).

Spatially-averaged SST errors are consistently lower over the year for *Tide* for the three regions (Philippine Sea, Kuroshio and SCS, Figures 5g–5i). In the Philippine Sea region (Figure 5g), SST errors are the lower than the Kuroshio and SCS regions (note the different *y*-axis scales), and *Tide* has only slightly lower errors by about 0.05°C than *No-Tide*. SST errors are largest in the Kurushio region (Figure 5h). In the summer and fall, *No-Tide* does much worse than *Tide* in its forecasts and analyses, and the *No-Tide* analyses provide significant reductions in error compared to the forecasts, which deviate rapidly over the 7-day windows. In the SCS (Figure 5i), *Tide* provides better SST estimates over most of the year, in particular after June. The period of poor SST predictability in *No-Tide* in the Kuroshio (Figure 5h) corresponds to period of poor SSH predictability in the same region (Figure 5e). This correspondence is also evident in the SCS, to a lesser extent (Figures 5f and 5i).
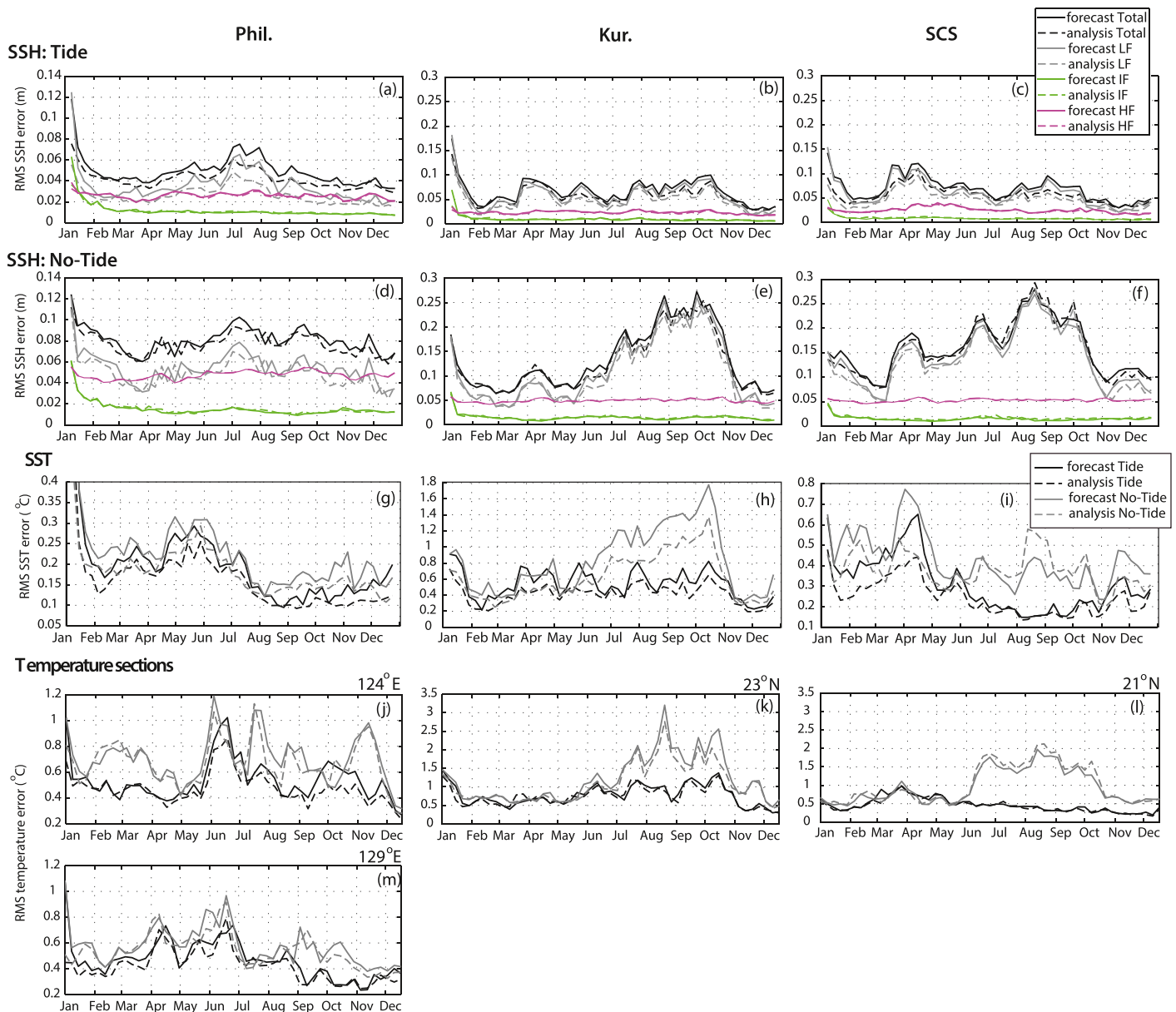
Figure 5. Time-series of spatially-averaged RMS Forecast and Analysis errors for low frequency components of Sea Surface Height for the Philippine Sea (Phil.), Kuroshio (Kur.) and South China Sea (SCS) regions for (a, b, and c) *Tide* and (d, e, and f) *No-Tide*. Note for *No-Tide* the TPXO7.1 tidal prediction is subtracted from the *Reference State* before comparison. Time-series of spatially-averaged RMS Forecast and Analysis errors for Sea Surface Temperature for the Philippine Sea, Kuroshio and SCS regions (g, h, and i). Regions are shown in Figure 4c. RMS Forecast and Analysis error for daily-averaged temperature cross-sections through (j) 124°E (17–12°N, upper 800 m), (k) 23°N (121–124°E, upper 800 m), (l) 21°N (120–122.5°E, all depths), and (m) 129°E (17–24°N, upper 800 m). Cross-section locations are shown in Figure 4e.

3.2.3. Subsurface Temperature

Comparisons of LF temperature fluctuations from *Tide* and *No-Tide* with the *Reference State* were performed at various depths, and the results are presented for the depth of 300 m, which is the typical thermocline depth and the depth of largest temperature variability (Figures 4e and 4f). LF analysis and forecast errors for temperature at 300 m (T_{300m}) are generally lower for *Tide* than *No-Tide*. In *Tide* the errors are highest over the SCS and in the Kuroshio (Figure 4e). The SCS errors are greatest to the north at the edge of the shallow shelf; dynamics in this region are likely to be highly nonlinear due to the large amplitude internal tides and the strong tidal velocities over
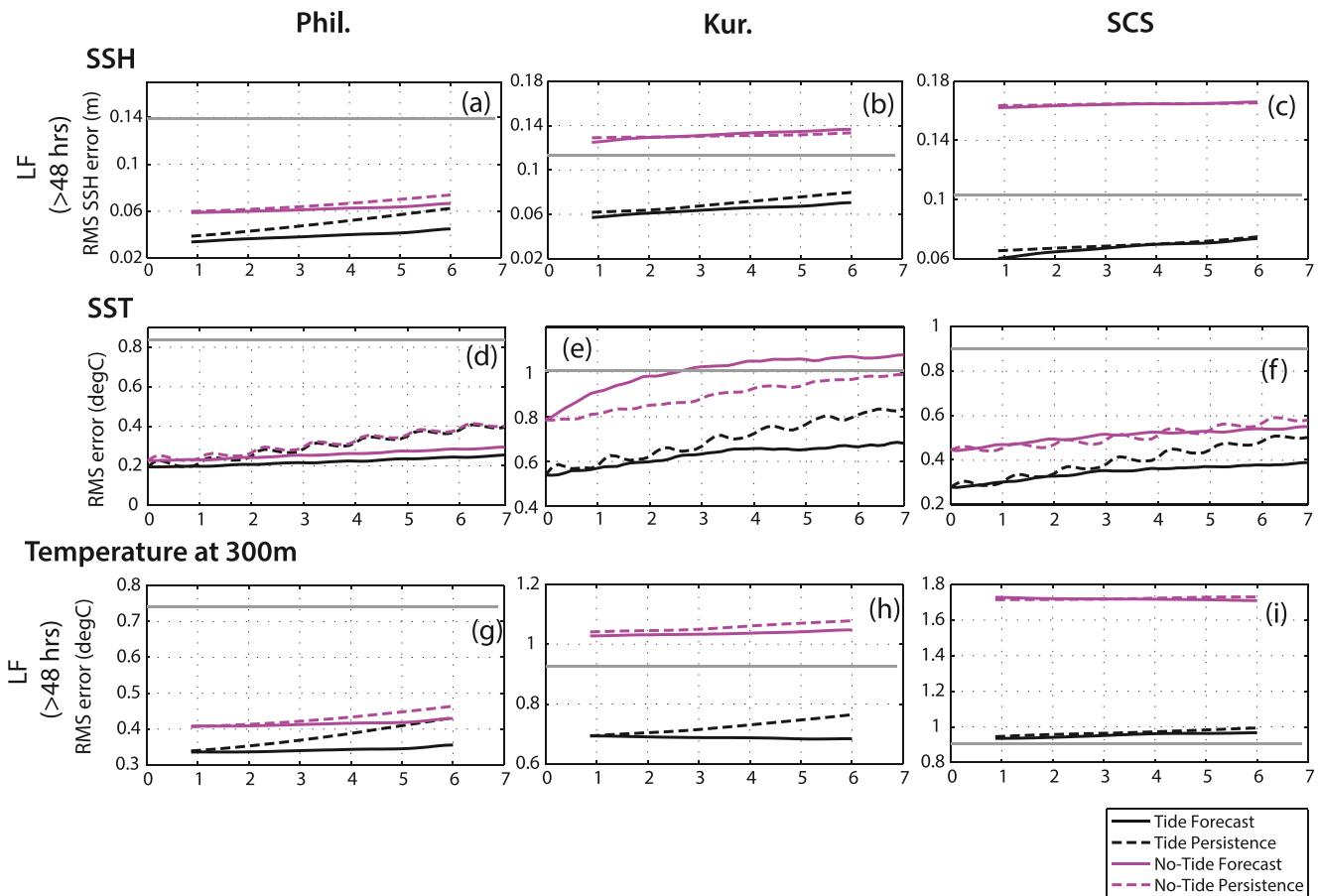
Figure 6. Root-mean squared error relative to the *Reference State* for each day of the 7-day forecast windows for the Philippine Sea (Phil.), Kuroshio (Kur.) and South China Sea regions (shown in Figure 4c), for the low frequency (LF) component of Sea Surface Height (SSH), Sea Surface Temperature, and the LF component of temperature at 300 m. The gray lines show the RMS anomaly over the year-long *Reference State* simulation (for SSH the tidal surface elevations predicted by TPXO7.1 are removed). The last 49 windows are used as the first 2 weeks of the 51 windows are not included due to large adjustments.

the shallow shelf (Alford et al., 2011, 2015; Li et al., 2020; Ramp et al., 2004). The properties of the Kuroshio are strongly controlled by the SCS waters (Rudnick et al., 2011; Wu et al., 2017; Yuan et al., 2006).

No-Tide LF errors are also highest in the northern SCS and the Kuroshio, and are elevated along the southern and eastern boundaries (Figure 4f). Both SST and T_{300m} are consistently cooled in the analysis compared to the forecast in this northern SCS region; the mean adjustment to the initial conditions over all assimilation periods is around 1°C for SST and 0.6°C for T_{300m} in this area (not shown). Adjustments in *Tide* are not biased, with mean upper ocean temperature adjustments close to zero in this region. This is because *Tide* captures the tidal dynamics that result in cooling of the upper ocean in the SCS and Kuroshio regions.

The LF subsurface temperature estimates have increased errors for the 21°N and 23°N cross sections (through the Luzon Strait and the Kuroshio, Figure 4e) in *No-Tide* (Figures 5k and 5l), corresponding to the poor SSH and SST estimates and predictions in summer and fall in the SCS and Kuroshio regions (Figures 5e, 5f, 5h, and 5i). For the cross sections in the Philippine Sea deep basin, through 124°E and 129°E (Figures 5j and 5m), *Tide* has lower errors in LF temperature in the upper 800 m over most of the year compared to *No-Tide* although the difference is less pronounced than for the sections to the west (Figures 5k and 5l, again note the different *y*-axis scales).

3.3. Predictive Skill

Comparison of the forecast errors as they evolve over the 7-day window demonstrates the predictive skill of the two experiments. As above, the SSH and T_{300m} outputs are filtered to show only the LF component. The spatial-

ly-averaged RMS difference between the forecast and the *Reference State* (forecast error) for the Philippine Sea, Kuroshio and SCS regions is plotted against days from the beginning of the forecast window, for both *Tide* and *No-Tide* (Figure 6). The model forecast error is compared to the error achieved when forecasts are made assuming persistence (i.e., no change in the ocean state) and to the RMS anomalies. *Tide* provides improved forecasts compared to *No-Tide* across all metrics and all three regions.

For SSH, tidal SSH predications from TPXO7.1 were subtracted from the *Tide* initial conditions for use in prediction based on persistence. Likewise, TPXO7.1 was subtracted from the *Reference State* for comparison with *No-Tide* predictions. *Tide* gives significantly better SSH predictions for the three regions than *No-Tide*. LF analysis errors in the Philippine Sea area are about 3 cm for *Tide* and increase only slightly to about 4 cm at the end of the 7-day assimilation window. *No-Tide* errors are higher at 6–7 cm but remain well below the RMS anomaly for the region (Figure 6a). In the Kuroshio and SCS however, *No-Tide* LF SSH forecast errors exceed the anomalies (Figures 6b and 6c).

SST forecast errors (Figures 6d–6f) show a small improvement in *Tide* compared to *No-Tide* in the Philippine Sea region, and significant improvement in the Kurushio and SCS regions. The anomalies presented for SST are the RMS of the seasonal anomalies. Forecasts in the Philippine Sea are well below the anomaly value for *Tide* and *No-Tide* (Figure 6d). *Tide* provides significantly better SST forecasts in the Kuroshio region, where the *No-Tide* forecasts are worse than persistence on average and exceed the anomalies after day 3 (Figure 6e). In the SCS, *Tide* and *No-Tide* forecast errors are both below the anomaly, and while *Tide* provides an improvement on persistence, *No-Tide* does not (Figure 6f). The persistence forecasts for SST do not capture the diurnal heating and cooling of the sea surface, resulting in diurnal fluctuations in the errors.

For T_{300m}, in the Philippine Sea and Kuroshio regions, the *Tide* forecast errors are below the anomalies and remain fairly constant over the forecast window, while the persistence errors increase over time (Figures 6g and 6h), indicating that the temporal evolution of the subsurface temperature is well represented in the model. In the SCS, the LF T_{300m} forecasts are poor; the errors are of the same order of magnitude as the anomaly for *Tide* and about twice the anomaly for *No-Tide* (Figure 6i).

In summary, *Tide* has consistently lower forecast errors than *No-Tide* for the subtidal flows as described by the LF variability of SSH, SST and T_{300m}. This is primarily due to improved state estimates (in Figure 6 the error at the initial time is always lower for *Tide* compared to *No-Tide*) but also due to the improved temporal evolution of LF, mesoscale eddy related features, as shown by the slower growth of the forecast errors compared to persistence. This is most notable in the SST forecasts in the Kuroshio and SCS regions, where *Tide* provides greater improvement compared to persistence than *No-Tide* indicating improved temporal evolution of the subtidal flows in the forecast model with tides.

4. Discussion of Mechanisms for Improvement by Including Tides

4.1. Tidal Mixing in the South China Sea

Estimates and predictions of SSH and surface and subsurface temperature are significantly worse in the SCS and Kuroshio regions when tides were not included in the simulation (*No-Tide*). The free-running forward model for 2010 with M_2 tides (the *Reference State*) has cooler surface temperatures over the shallow SCS shelf and cooler water at 300 m in the SCS basin compared to a forward model without tides (Figures 4g and 4h). Full-column mixing occurs on the shallow SCS shelf when the tides are included in the model. Cooler subsurface temperatures in the region directly west of the Luzon Strait likely result from advection of these cooler, well-mixed waters, off of the shelf into the SCS. Vertical mixing induced by the dissipation of large amplitude internal tides may also play a role in the SCS. Li et al. (2020) showed that tidally-induced mixing is an important dynamic that controls the temperature of the upper ocean in these regions, as the cooler, deep waters are mixed with the warmer, surface waters.

Upper ocean temperatures are also cooler in the Kuroshio region when tides are included in the model (Figures 4g and 4h). Rather than direct tidal mixing in the Kuroshio, advection of the cooler SCS waters likely plays an important role. The Kuroshio flows northward from the Luzon Strait adjacent to the east coast of Taiwan (Andres et al., 2015). We performed an adjoint sensitivity study (not shown) to examine the sensitivity of SST in the Kuroshio and found that this metric is sensitive to upper ocean temperature in the SCS. This is consistent with

Chen (2005) and Mensah et al. (2014) who demonstrate significant modification of the Kuroshio Tropical Water at the Luzon Strait and suggest that this is due to mixing of the Kuroshio and SCS Tropical Water on the Kuroshio's western side. The dissipation of internal tides is likely to play a key role in the mixing of these water masses in the Luzon Strait.

Increased vertical mixing in the presence of tides in the model may be attributed to increased velocity shear and therefore increased explicit diffusion, as well as increased implicit sub-grid scale dissipation. In the SCS region the tides could result in enhanced vertical mixing due to (a) the enhanced velocity shear associated with barotropic tidal flow over the shallow shelf and (b) the dissipation of the baroclinic tides. In this study, the horizontal mixing is handled using a harmonic (3-point stencil) mixing operator (D. Haidvogel & Beckmann, 1999) and the viscosity is derived from the horizontal divergence of the deviatory stress tensor (Wajsowicz, 1993). Vertical turbulent mixing of momentum and tracers is parameterized using the Mellor and Yamada (1982) level-2.5, second-moment turbulence closure scheme (MY2.5). In this closure scheme, the turbulent kinetic energy equation relates the vertical diffusion of turbulent kinetic energy to the horizontal velocity shear, buoyancy and dissipation. Kerry et al. (2014b) show that internal tide induced depth-mean turbulent diffusivity is 5–20 times greater in the Luzon Starit and SCS regions than in the Philippine Sea deep basin. In the model, diffusivity near the Luzon Strait is dominated by high-mode internal tides associated with the dissipation of locally generated internal tides, and is enhanced upon interaction with the Loop Current in the SCS. While model estimates of mixing are uncertain because of the parameterization of sub-grid scale processes, Kerry et al. (2014b) show their model estimates of diffusivity in the Luzon Strait are consistent with observations.

4.2. Energetics in the Philippine Sea Deep Basin

While including the tides in our model had a significant impact on the predictability of the LF (mesoscale) ocean circulation in the Philippine Sea (Sections 3.2 and 3.3), we show that in the Philippine Sea deep basin the LF circulation energetics are not significantly influenced by the tides. The energy present at various length scales for the *Reference State*, *Tide* and *No-Tide* is presented through the surface kinetic energy spectra with zonal wave number for the Philippine Sea basin (Figure 7). The wave number spectra are calculated daily for each row of model grid cells and are then averaged in time and over the model's latitudinal extent. The zonal wave number spectra are presented as the internal tide and eddy propagation occur primarily in the zonal direction in this region. The total, high frequency (<2 days) and LF (>2 days) spectra are presented. Note that the high frequency component here is defined as periods less than 2 days (comprising both the intermediate and high frequency components that were defined in the above sections).

The *Tide* total and high frequency spectra match the *Reference State* well. Peaks in the high frequency spectra are seen at wave numbers associated with the Mode-1 and Mode-2 internal tides. *No-Tide* has lower surface kinetic energy in the high frequency range over the entire wavenumber range (less than ~500 km, Figure 7b). This reveals that scattering of the tides spreads the (high frequency) tidal energy out in wavenumber space.

The LF spectra, representing the mesoscale flows, for both *Tide* and *No-Tide* match the *Reference State* very well (Figure 7c). The best-fit slope of −2.55 over the mesoscale wavenumber band (corresponding to length scales of 70–250 km) is shown on this plot. This slope is between the −5/3 and −3 spectral slopes which imply surface quasi-geostophic and quais-geostrophic dynamics, respectively (Xu & Fu, 2011). This match of the LF surface kinetic energy spectra for *Tide* and *No-Tide* implies that the tides are not affecting the mean LF (surface) energetics in the Philippine Sea basin. While there is clear evidence of an inverse energy cascade (i.e., a spectral transfer of kinetic energy in wavenumber space) in the western tropical Pacific (Zedler et al., 2019) and the extratropics (Scott & Wang, 2005) at scales from the first baroclinic Rossby deformation radius to the basin scale, the transfer of energy in frequency (i.e., from tidal motions to LF flows) requires further study.

The time-mean LF kinetic energy profiles, spatially-averaged over the region of elevated mesoscale variability in the Philippine Sea (shown in Figure 4c), also match well for both *Tide* and *No-Tide* (Figure 7d), while the RMS errors are greater for *No-Tide* in the upper 250 m (Figure 7e). This indicates that the mean LF dynamics are not significantly affected by the tides in our simulations; however, the predictions of the temporal evolution of the LF dynamics (in the upper 250 m) are worse when the tides are not included.

While the tides do not impact the time-mean mesoscale dynamics in the Philippine Sea deep basin, including the tides in our model provides significant improvement in the estimates of the temporal evolution of the LF (mesos-
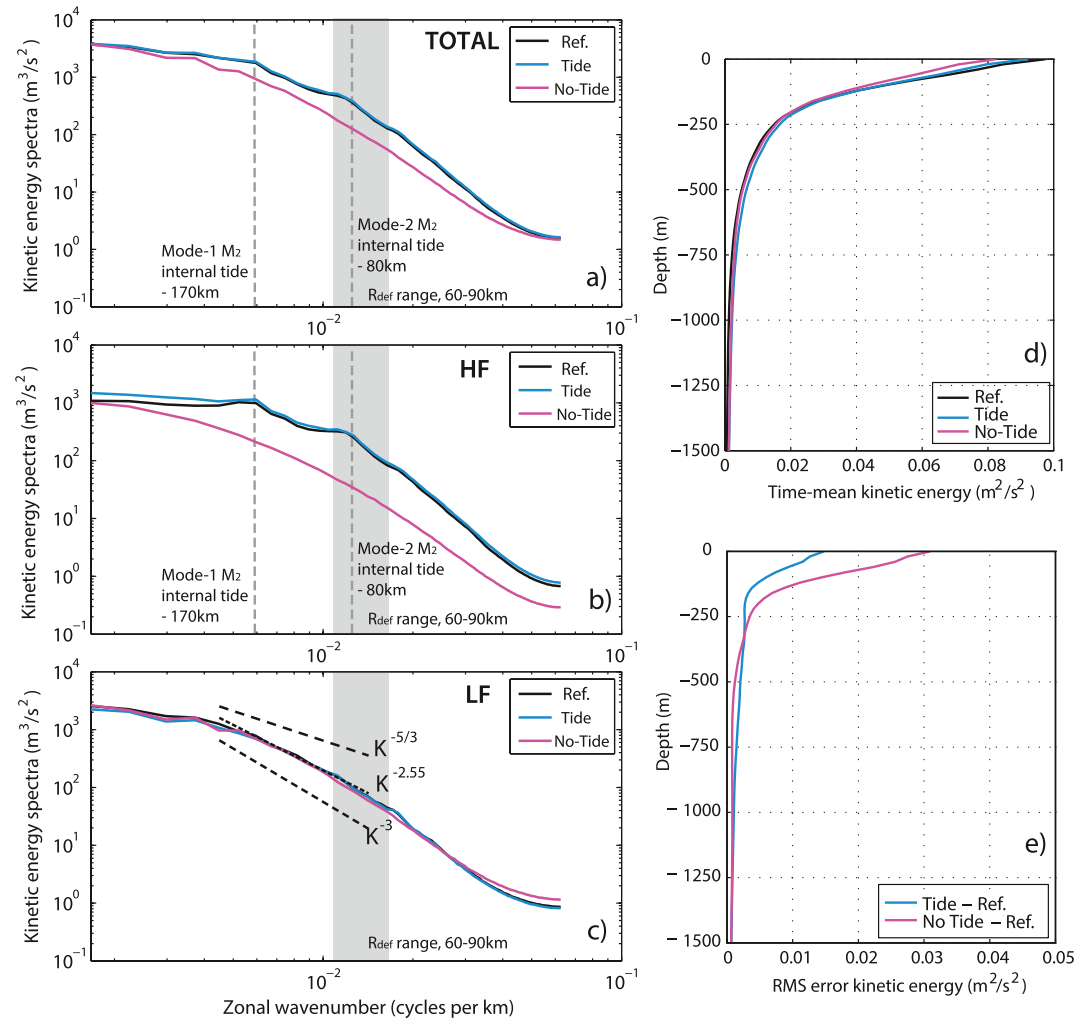
Figure 7. Comparison of *Reference State Tide* and *No-Tide* zonal wavenumber surface kinetic energy spectra across the Philippine Sea basin for (a) total, (b) high frequency (<2 days) and (c) low frequency (LF) (>2 days) components. The length scales of the Mode-1 and Mode-2 M_2 internal tides are shown by the vertical dashed lines and the range of length scales associated with the Rossby radius of deformation (R_{def}) for the domain's latitudinal range is shaded in gray. The spectral slope is shown on the LF spectra for the 70–250 km mesoscale range with the −5/3 and −3 slopes shown for comparison. (d) Time-mean and (e) RMS error of the 7-day mean, spatially-averaged kinetic energy profiles over the Philippine Sea area (Figure 4c) for the last 49 (of 51) assimilation windows.

cale) ocean circulation. Specifically, the time-mean LF energetics (as described by the kinetic energy spectra in Figure 7c and the kinetic energy profiles in Figure 7d) are not affected by the tides in the Philippine Sea deep basin; however, prediction of the LF SSH (and hence geostrophic velocities) and temperature are worse without tides (Figures 6a and 6g), and the temporal evolution of the kinetic energy in the upper 250 m is worse in the absence of tides (Figure 7e).

These degraded estimates come about as there is greater uncertainty in the SSH (Figure 2c) and the subsurface temperature and salinity observations (Figures 2f and 2g) when the internal tides are not resolved. Not resolving the internal tides in *No-Tide* reduces the value of subsurface observations, particularly about the thermocline, as we must specify large prior errors about the observations to account for the vertical displacements associated with the internal tides that are sampled by the observations but not captured by the model. Likewise, SSH observations in *No-Tide* have higher prior errors due to the unresolved internal tide surface expression (Figure 2c), and SSH predictions are worse in *No-Tide* than in *Tide*. SSH is strongly correlated to the thermal structure of the upper ocean (Goni et al. (1996) and verified for this study). Both the SSH and the subsurface temperature (and salinity) are less constrained to observations in *No-Tide*, and these variables are dynamically connected. This results in
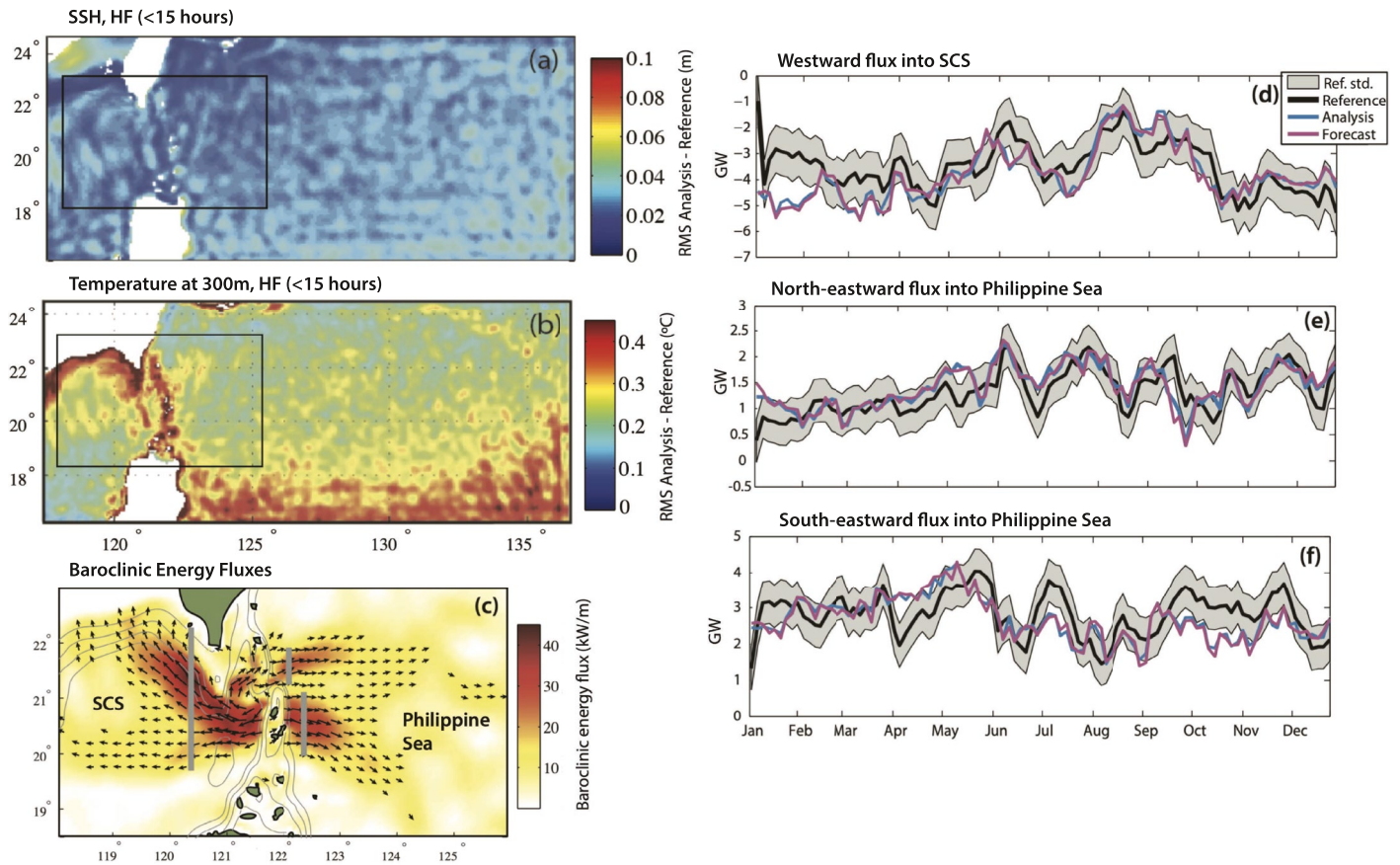
Figure 8. Root-mean squared Analysis-*Reference State* for high frequencies (a) Sea Surface Height and (b) temperature at 300 m for *Tide*. (c) Time-mean M_2 baroclinic energy flux vectors (only shown for magnitudes greater than 10 kW/m) for fluxes calculated every 3.5 days from the *Reference State* over region shown by black box in panel (b). M_2 baroclinic energy fluxes integrated across the sections shown by the gray lines in panel (c), corresponding to the dominant internal tide beams (d) westward into the South China Sea, (e) north-eastward into the Philippine Sea and (f) south-eastward into the Philippine Sea. The fluxes are calculated every 3.5 days from the *Reference State*, *Tide* forecast and *Tide* analysis. The gray shaded area shows the standard deviation in the *Reference State* fluxes over the year.

greater analysis and forecast errors for SSH and surface and subsurface temperature in *No-Tide* over the deep Philippine Sea basin. Given the dynamical connection between SSH, the three-dimensional density structure of the ocean and ocean's velocity structure, resolving the tides is crucial to accurate state estimates and predictions of the subtidal ocean circulation.

4.3. Reduction of Observation Errors Through Resolution of the Internal Tides

Due to the spatial and temporal variability of the internal tides, estimating the error associated with the unresolved internal tides is indeed complex. In this study we apply lower errors to SSH and subsurface temperature and salinity for the model with tides, as we are reducing the observational uncertainty by resolving the internal tides. The reduction in prior observation errors for *Tide* compared to *No-Tide* makes the assumption that *Tide* performs well in estimating the internal tides and their associated SSH expression and isotherm heave.

At HF (periods < 15 hr) we observe the ability of *Tide* to capture the surface expression of the M_2 internal tides well (Figure 8a). For *Tide* the HF analysis errors are of the order of 1–3 cm over most of the domain, with slightly higher errors of ∼4 cm in the south-east of the domain where the internal tides from the Mariana Arc have more of an influence. These errors are small relative to the amplitude of the SSH internal tide expression (refer to Figure 2c which represents the mean internal tide SSH expression as explained in Section 2.3.2). Estimates of the isotherm displacement in *Tide* (Figure 8b) have the highest errors directly over the Luzon Strait internal tide generation sites, along the edge of the continental shelf in the SCS, and in the southern portion of the domain. Internal tides in the southern portion of the domain originate mostly from the Mariana Arc generation site, which

are imposed at the boundaries of the *Inner* domain from the free-running *Outer* model. Without assimilation to constrain the mesoscale field that influences the generation and propagation of internal tides from the Mariana Arc, the errors in internal tide representation are higher here. The HF forecast errors (not shown) are of similar magnitude to the analysis errors indicating that the *Tide* model performs well in predicting the internal tides across the domain. This is expected as changes in the internal tide generation, propagation and dissipation are driven by the mesoscale circulation (Kerry et al., 2014a, 2014b), which varies little on time scales of 7 days.

The M_2 baroclinic energy fluxes emanating from the Luzon Strait in the westward beam, and in the northern and southern eastward beams for *Tide* are compared to the *Reference State* fluxes in Figures 8d–8f. The zonal energy fluxes are integrated across the meridional sections shown by the gray lines in Figure 8c, to capture the dominant flux beams. An initial adjustment period of 1–2 months is seen in all three plots, over which the stratification over the generation site adjusts to better match the *Reference State* and the flux predictions become closer to the *Reference State*. After this initial period, the flux into the SCS is well represented in the *Tide* experiment (Figure 8d). The north-eastern flux is also well predicted in the assimilation (Figure 8e), while the southern east-ward flux is less well represented (Figure 8f) with the analysis fluxes falling outside of one standard deviation from the *Reference State* fluxes 43% of the time excluding the first 2 months (compared to 16% for fluxes into the SCS (Figure 8d) and 20% for the northeastward beam (Figure 8e)). The internal tide generation over the eastern slope of the eastern ridge, from which this southern eastward flux emanates, was found to be the most sensitive to changes in the pressure perturbation at the ocean bottom, compared to the other regions of the generation site (Kerry et al., 2014a), therefore higher errors in flux estimates are expected. The remotely generated internal tides from the Mariana Arc were also found to have the greatest influence on generation variability over this generation slope region; these remote waves are not accurately predicted as we do not assimilate in the *Outer* model. Overall, these results show that *Tide* predicts the internal tides well providing confidence that our specified smaller observation errors about the SSH and in-situ observations are appropriate.

4.4. Sensitivity to Prior Error Choices

The performance of a data assimilation system depends strongly on the prior estimates of background and observation errors. When including tides we reduce the observation uncertainty associated with the internal tide expression. While various methods can be used to estimate the prior observation errors, in this study we have attempted to realistically estimate the observational errors and how they differ given a dynamical model that does or does not resolve the observed tidal signal. As such we believe that the comparisons between the two experiments are realistic and robust, given the limitations of the Twin Experiment framework.

A caveat of the methodology is that the same model (resolution, surface, boundary and tidal forcing) is used for the *Reference State* as for the assimilation experiments. As such, once the mesoscale circulation is well constrained, the model predictions of the internal tides match very well to the *Reference State*. In a realistic data assimilation system, the differences in model predictions and the true internal tides are likely to be greater as models are unable to fully resolve the steep topography associated with the internal tide generation sites, the internal waves from remote sources, as well as other wave–wave interactions. While these unresolved processes need to be accounted for in the observation errors, a model that resolves the tides will never-the-less be able to afford lower observation errors for SSH and subsurface observations about the thermocline compared to a model without tides.

5. Conclusions

The numerical prediction of oceanic regions with dynamic mesoscale circulation and strong internal tides presents a challenging task, and this study aims to further our understanding of how mesoscale and internal tide interactions influence the predictability of such dynamically rich regions. Focusing on the Philippine Sea, we assess how well we are able to predict the subtidal dynamics through the assimilation of a variety of observations into a numerical model that resolves the tides, and a numerical model that omits tidal forcing.

The study reveals that including tides improves subtidal circulation prediction across the region. The result is two-fold: firstly, tidal dynamics influence the subtidal circulation, and secondly, higher prior errors must be prescribed to the observations if the model does not resolve the internal tide signal. Tidally-induced mixing in the SCS results in cooling of the upper ocean, and advection of the SCS waters result is cooler Kuroshio waters

(compared to when the tides are not included in the simulation). Resolving this tidally-induced mixing in the SCS is crucial to predicting temperature in the Kuroshio, particularly in summer. In the Philippine Sea deep basin, tides do not impact the mesoscale dynamics but resolving the internal tides allows smaller prior errors to be prescribed to the assimilated SSH and subsurface observations. This allows the state estimates to be more tightly constrained by the observations, resulting in improved state estimates and predictions of the subtidal circulation.

The performance of a data assimilative prediction system is dependent on the prior choices of background and observation errors and in this study we have attempted to make realistic estimates of the prior errors. Specifically, the observation errors were adjusted to account for the resolution, or not, of the internal tides in the dynamical model. We focused on the dominant semidiurnal constituent, M_2, so as to be able to present a thorough analysis within the scope of this study. The M_2 and K_1 tidal constituents are both of approximately equal magnitude in the region (Alford et al., 2011; Zu et al., 2008) so the impact of tides is likely to be greater than shown and further studies may investigate the K_1 internal tides or combined constituents. These results are relevant across regions globally and should be considered when developing future prediction systems.

Data Availability Statement

A subset of the model output has been published to Research Data Australia (Kerry & Powell 2022, A free-running Regional Ocean Modeling System simulation that resolves the M_2 surface and internal tides and the varying sub-tidal circulation in the Philippine Sea for 2010). All model output is archived at Uni. Hawaii and can be made available for research purposes upon request.

References

Alford, M. H., MacKinnon, J. A., Nash, J. D., Simmons, H., Pickering, A., Klymak, J. M., et al. (2011). Energy flux and dissipation in Luzon Strait: Two tales of two ridges. *Journal of Physical Oceanography*, *41*(11), 2211–2222. https://doi.org/10.1175/jpo-d-11-073.1

Alford, M. H., Peacock, T., MacKinnon, J. A., Nash, J. D., Buijsman, M. C., Centuroni, L. R., et al. (2015). The formation and fate of internal waves in the South China Sea. *Nature*, *521*(7550), 65–69. https://doi.org/10.1038/nature14399

Andres, M., Jan, S., Sanford, T., Mensah, V., Centurioni, L., & Book, J. (2015). Mean structure and variability of the Kuroshio from northeastern Taiwan to southwestern Japan. *Oceanography*, *28*(4), 84–95. https://doi.org/10.5670/oceanog.2015.84

Arbic, B. K., Wallcraft, A. J., & Metzger, E. J. (2010). Concurrent simulation of the eddying general circulation and tides in a global ocean model. *Ocean Modelling*, *32*(3–4), 175–187. https://doi.org/10.1016/j.ocemod.2010.01.007

Bergh, J., & Berntsen, J. (2009). Numerical studies of wind forced internal waves with a nonhydrostatic model. *Ocean Dynamics*, *59*(6), 1025–1041. https://doi.org/10.1007/s10236-009-0226-1

Chassignet, E., Hurlburt, H., Metzger, E., Smedstad, O., Cummings, J., Halliwell, G., et al. (2009). Global ocean prediction with the hybrid coordinate ocean model (HYCOM). *Oceanography*, *22*(2), 64–75. https://doi.org/10.5670/oceanog.2009.39

Chen, C. T. A. (2005). Tracing tropical and intermediate waters from the South China Sea to the Okinawa Trough and beyond. *Journal of Geophysical Research*, *110*(C5), C05012. https://doi.org/10.1029/2004jc002494

CNES. (2015). *SSALTO/DUACS user handbook: (M)SLA and (M)ADT near-real time and delayed time products*. AVISO Sateliitle Altimetry Data.

Courtier, P., Thepaut, J. N., & Hollingsworth, A. (1994). A strategy for operational implementation of 4D-Var, using an incremental approach. *Quarterly Journal of the Royal Meteorological Society*, *120*(519), 1367–1387. https://doi.org/10.1002/qj.49712051912

Di Lorenzo, E., Moore, A. M., Arango, H. G., Cornuelle, B., Miller, A. J., Powell, B. S., et al. (2007). Weak and strong constraint data assimilation in the inverse Regional Ocean Modelling System (ROMS): Development and application for a baroclinic coastal upwelling system. *Ocean Modelling*, *16*(3–4), 160–187. https://doi.org/10.1016/j.ocemod.2006.08.002

Di Lorenzo, E., Young, W. R., & Smith, S. L. (2006). Numerical and analytical estimates of M_2 tidal conversion at steep oceanic ridges. *Journal of Physical Oceanography*, *36*(6), 1072–1084. https://doi.org/10.1175/jpo2880.1

Egbert, G. D., & Erofeeva, S. Y. (2002). Efficient inverse modeling of barotropic ocean tides. *Journal of Atmospheric and Oceanic Technology*, *19*(2), 183–204. https://doi.org/10.1175/1520-0426(2002)019<0183:eimobo>2.0.co;2

Goni, G., Kamholz, S., Garzoli, S., & Olson, D. (1996). Dynamics of the Brazil-Malvinas Conuence based on inverted echo sounders and altimetry. *Journal of Geophysical Research*, *101*(C7), 16273–16289. https://doi.org/10.1029/96jc01146

Gopalakrishnan, G., Cornuelle, B., Mazloff, M., Worcester, P., & Dzieciuch, M. (2021a). State estimates and forecasts of the eddy field in the subtropical countercurrent in the northern Philippine Sea. *Journal of Atmospheric and Oceanic Technology*, *38*, 1889–1911. https://doi.org/10.1175/JTECH-D-20-0083.1

Gopalakrishnan, G., Cornuelle, B., Mazloff, M., Worcester, P., & Dzieciuch, M. (2021b). State estimates and forecasts of the northern Philippine Sea circulation including ocean acoustic travel times. *Journal of Atmospheric and Oceanic Technology*, *38*, 1913–1933. https://doi.org/10.1175/JTECH-D-20-0178.1

Haidvogel, D., & Beckmann, A. (1999). *Numerical Ocean circulation modeling*. Imperial College Press. https://doi.org/10.1142/p097

Haidvogel, D. B., Arango, H. G., Hedstrom, K., Beckmann, A., Malanotte-Rizzoli, P., & Shchepetkin, A. F. (2000). Model evaluation experiments in the North Atlantic Basin: Simulations in nonlinear terrain-following coordinates. *Dynamics of Atmospheres and Oceans*, *32*(3–4), 239–281. https://doi.org/10.1016/s0377-0265(00)00049-x

Haney, R. L. (1991). On the pressure gradient force over steep topography in sigma coordinate ocean models. *Journal of Physical Oceanography*, *21*(4), 610–619. https://doi.org/10.1175/1520-0485(1991)021<0610:otpgfo>2.0.co;2

Houtekamer, P. L., & Mitchel, H. L. (1998). Data assimilation using an ensemble Kalman filter technique. *Monthly Weather Review*, *126*, 796–811.

IOC, IHO, & BODC. (2003). *Centenary edition of the GEBCO digital atlas, published on CD-ROM on behalf of the intergovernmental oceanographic commission and the international hydrographic organization as part of the general bathymetric Chart of the Oceans*. British Oceanographic Data Centre.

Janekovic, I., & Powell, B. (2012). Analysis of imposing tidal dynamics to nested numerical models. *Continental Shelf Research*, *34*, 30–40. https://doi.org/10.1016/j.csr.2011.11.017

Kerry, C., & Powell, B. (2022). *A free-running Regional Ocean Modelling System simulation that resolves the M2 surface and internal tides and the varying sub-tidal circulation in the Philippine Sea for 2010*. https://doi.org/10.26190/unsworks/23905

Kerry, C. G., Powell, B. S., & Carter, G. S. (2013). Effects of remote generation sites on model estimates of M_2 internal tides in the Philippine Sea. *Journal of Physical Oceanography*, *43*(1), 187–204. https://doi.org/10.1175/jpo-d-12-081.1

Kerry, C. G., Powell, B. S., & Carter, G. S. (2014a). The impact of subtidal circulation on internal tide generation and propagation in the Philippine Sea. *Journal of Physical Oceanography*, *44*(5), 1386–1405. https://doi.org/10.1175/jpo-d-13-0142.1

Kerry, C. G., Powell, B. S., & Carter, G. S. (2014b). The impact of subtidal circulation on internal-tide-induced mixing in the Philippine Sea. *Journal of Physical Oceanography*, *44*(12), 3209–3224. https://doi.org/10.1175/jpo-d-13-0249.1

Kerry, C. G., Powell, B. S., & Carter, G. S. (2016). Quantifying the incoherent M_2 internal tide in the Philippine Sea. *Journal of Physical Oceanography*, *46*(8), 2483–2491. https://doi.org/10.1175/jpo-d-16-0023.1

Kerry, C. G., Powell, B. S., Roughan, M., & Oke, P. R. (2016). Development and evaluation of a high-resolution reanalysis of the East Australian Current region using the Regional Ocean Modelling System (ROMS 3.4) and Incremental Strong-Constraint 4-Dimensional Variational (IS4D-Var) data assimilation. *Geoscientific Model Development*, *9*(10), 3779–3801. https://doi.org/10.5194/gmd-9-3779-2016

Kistler, R., Kalnay, E., Collins, W., Saha, S., Woollen, J., White, G., et al. (2001). The NCEP/NCAR 50-year reanalysis. *Bulletin of the American Meteorological society*, *82*(2), 247–268. https://doi.org/10.1175/1520-0477(2001)082<0247:tnnyrm>2.3.co;2

Li, Y., Curchitser, E. N., Wang, J., & Peng, S. (2020). Tidal effects on the surface water cooling northeast of Hainan Island, South China Sea. *Journal of Geophysical Research: Oceans*, *125*(10), e2019JC016016. https://doi.org/10.1029/2019jc016016

Lien, R. C., Ma, B., Cheng, Y. H., Ho, C. R., Qiu, B., Lee, C. M., & Chang, M. H. (2014). Modulation of Kuroshio transport by mesoscale eddies at the Luzon Strait entrance. *Journal of Geophysical Research: Oceans*, *119*(4), 2129–2142. https://doi.org/10.1002/2013jc009548

Mellor, G. L., Ezer, T., & Oey, L. Y. (1994). The pressure gradient error conundrum of sigma coordinate ocean models. *Journal of Atmospheric and Oceanic Technology*, *11*(4), 1126–1134. https://doi.org/10.1175/1520-0426(1994)011<1126:tpgcos>2.0.co;2

Mellor, G. L., & Yamada, T. (1982). Development of a turbulence closure model for geophysical fluid problems. *Reviews of Geophysics and Space Physics*, *20*(4), 851–875. https://doi.org/10.1029/rg020i004p00851

Mensah, V., Jan, S., Chiou, M. D., Kuo, T. H., & Lien, R. C. (2014). Evolution of the Kuroshio Tropical Water from the Luzon Strait to the east of Taiwan. *Deep-Sea Research I*, *86*, 68–81. https://doi.org/10.1016/j.dsr.2014.01.005

Moore, A. M., Arango, H. G., Broquet, G., Powell, B. S., Zavala-Garay, J., & Weaver, A. T. (2011). The Regional Ocean Modeling System (ROMS) 4-dimensional variational data assimilation systems: Part I – System overview and formulation. *Progress in Oceanography*, *91*(1), 34–49. https://doi.org/10.1016/j.pocean.2011.05.004

Moore, A. M., Arango, H. G., Di Lorenzo, E., Cornuelle, B. D., Miller, A. J., & Neilson, D. J. (2004). A comprehensive ocean prediction and analysis system based on the tangent linear and adjoint of a regional ocean model. *Ocean Modelling*, *7*(1–2), 227–258. https://doi.org/10.1016/j.ocemod.2003.11.001

Oke, P. R., Brassington, G. B., Griffin, D. A., & Schiller, A. (2008). The Bluelink ocean data assimilation system (BODAS). *Ocean Modelling*, *21*(1–2), 46–70. https://doi.org/10.1016/j.ocemod.2007.11.002

Oke, P. R., Schiller, A., Griffin, D. A., & Brassington, G. B. (2005). Ensemble data assimilation for an eddy-resolving ocean model of the Australian region. *Quarterly Journal of the Royal Meteorological Society*, *131*(613), 3301–3311. https://doi.org/10.1256/qj.05.95

Pickering, A., Alford, M., Nash, J., Rainville, L., Buijsman, M., DongKo, S., & Lim, B. (2015). Structure and variability of internal tides in Luzon Strait. *Journal of Physical Oceanography*, *45*(6), 1574–1594. https://doi.org/10.1175/jpo-d-14-0250.1

Powell, B. S., Arango, H. G., Moore, A. M., Di Lorenzo, E., Milliff, R. F., & Foley, D. (2008). 4DVAR data assimilation in the intra-Americas sea with the Regional Ocean Modeling System (ROMS). *Ocean Modelling*, *25*(3–4), 173–188. https://doi.org/10.1016/j.ocemod.2008.08.002

Qiu, B., & Chen, S. (2010). Interannual variability of the North Pacific Subtropical Countercurrent and its associated mesoscale eddy field. *Journal of Physical Oceanography*, *40*(1), 213–225. https://doi.org/10.1175/2009jpo4285.1

Qiu, B., Chen, S., & Carter, G. S. (2012). Time-varying parametric subharmonic instability from repeat CTD surveys in the northwestern Pacific Ocean. *Journal of Geophysical Research*, *117*(C9), 1–12. https://doi.org/10.1029/2012jc007882

Ramp, S. R., Tang, T. Y., Duda, T. F., Lynch, J. F., Liu, A. K., Chiu, C. S., et al. (2004). Internal solitons in the northeastern South China Sea Part 1: Sources and deep water propogation. *Journal of Oceanic Engineering*, *29*(4), 1157–1181. https://doi.org/10.1109/joe.2004.840839

Rudnick, D. L., Jan, S., Centurioni, L., Lee, C. M., Wang, J., Lee, D. K., et al. (2011). Seasonal and mesoscale variability of the Kuroshio near its origin. *Oceanography*, *24*(4), 52–63. https://doi.org/10.5670/oceanog.2011.94

Scott, R. B., & Wang, F. (2005). Direct evidence of an oceanic inverse kinetic energy cascade from satellite altimetry. *Journal of Physical Oceanography*, *35*, 1650–1666. https://doi.org/10.1175/JPO2771.1

Shchepetkin, A. F., & McWilliams, J. C. (1998). Quasi-monotone advection schemes based on explicit locally adaptive dissipation. *Monthly Weather Review*, *126*(6), 1541–1580. https://doi.org/10.1175/1520-0493(1998)126<1541:qmasbo>2.0.co;2

Shchepetkin, A. F., & McWilliams, J. C. (2003). A method for computing horizontal pressure-gradient force in an oceanic model with a nonaligned vertical coordinate. *Journal of Geophysical Research*, *108*(C3), 3090. https://doi.org/10.1029/2001jc001047

Shchepetkin, A. F., & McWilliams, J. C. (2005). The Regional Oceanic Modeling System (ROMS): A split-explicit, free-surface, topography-following-coordinate oceanic model. *Ocean Modelling*, *9*(4), 347–404. https://doi.org/10.1016/j.ocemod.2004.08.002

Shriver, J. F., Arbic, B. K., Richman, J. G., Ray, R. D., Metzger, E. J., Wallcraft, A. J., & Timko, P. G. (2012). An evaluation of the barotropic and internal tides in a high-resolution global ocean circulation model. *Journal of Geophysical Research*, *117*(C10), 1–14. https://doi.org/10.1029/2012jc008170

Shriver, J. F., Richman, J. G., & Arbic, B. K. (2014). How stationary are the internal tides in a high-resolution global ocean circulation model? *Journal of Geophysical Research*, *119*(5), 2769–2787. https://doi.org/10.1002/2013jc009423

Sikiric, M. D., Janekovic, I., & Kuzmic, M. (2009). A new approach to bathymetry smoothing in sigma-coordinate ocean models. *Ocean Modelling*, *29*(2), 128–136. https://doi.org/10.1016/j.ocemod.2009.03.009

Simmons, H. L., Hallberg, R. W., & Arbic, B. K. (2004). Internal wave generation in a global baroclinic tide model. *Deep-Sea Research II*, *51*(25–26), 3043–3068. https://doi.org/10.1016/j.dsr2.2004.09.015

Souza, J., Powell, B. S., Castillo-Trujillo, A. C., & Flament, P. (2014). The vorticity balance of the ocean surface in Hawaii from a regional reanalysis. *Journal of Physical Oceanography*, *45*, 424–440.

Stark, J., Donlon, C., Martin, M., & McCulloch, M. (2007). *OSTIA : An operational, high resolution, real time, global sea surface temperature analysis system*. Oceans 07 IEEE Aberdeen. conference proceedings. https://doi.org/10.1109/oceanse.2007.4302251

Thoppil, P., Frolov, S., Rowley, C., Reynolds, C., Jacobs, G., Metzger, E., et al. (2021). Ensemble forecasting greatly expands the prediction horizon for ocean mesoscale variability. *Nature Communications Earth and Environment*, *2*(1), 89. https://doi.org/10.1038/s43247-021-00151-5

Vitousek, S., & Fringer, O. B. (2011). Physical vs. numerical dispersion in nonhydrostatic ocean modeling. *Ocean Modelling*, *40*, 72–86. https://doi.org/10.1016/j.ocemod.2011.07.002

Wajsowicz, R. C. (1993). A consistent formulation of the anisotropic stress tensor for use in models of the large-scale ocean circulation. *Journal of Computational Physics*, *105*(2), 333–338. https://doi.org/10.1006/jcph.1993.1079

Weaver, A., & Courtier, P. (2001). Correlation modelling on the sphere using generalized diffusion equation. *Quarterly Journal of the Royal Meteorological Society*, *127*, 1815–1846.

Worcester, P., Andrew, R., Baggeroer, A., Colosi, J., D'Spain, G., Dzieciuch, M., et al. (2012). The North Pacific Acoustic Laboratory (NPAL) deep-water acoustic propagation experiments in the Philippine Sea. *Journal of the Acoustical Society of America*, *131*(4), 3352. https://doi.org/10.1121/1.4708562

Wu, C. R., Wang, Y. L., Lin, Y. F., & Chao, S. Y. (2017). Intrusion of the Kuroshio into the south and East China seas. *Scientific Reports*, *7*, 1–8. https://doi.org/10.1038/s41598-017-08206-4

Xu, Y., & Fu, L. L. (2011). Global variability of the wavenumber spectrum of oceanic mesoscale turbulence. *Journal of Physical Oceanography*, *41*(4), 802–809. https://doi.org/10.1175/2010jpo4558.1

Yuan, D., Han, W., & Hu, D. (2006). Surface Kuroshio path in the Luzon Strait area derived from satellite remote sensing data. *Journal of Geophysical Research*, *111*(C11), 1–16. https://doi.org/10.1029/2005jc003412

Zedler, S. E., Powell, B. S., Qiu, B., & Rudnick, D. L. (2019). Energy transfer in the western tropical Pacific. *Oceanography*, *32*(4), 136–145. https://doi.org/10.5670/oceanog.2019.419

Zu, T., Gan, J., & Erofeeva, S. Y. (2008). Numerical study of the tide and tidal dynamics in the South China Sea. *Deep-Sea Research II*, *55*(2), 137–154. https://doi.org/10.1016/j.dsr.2007.10.007